

---

# Disentangling the stellar inclination of transiting planetary systems: fully analytic approach to the Rossiter-McLaughlin effect incorporating the stellar differential rotation

Shin SASAKI<sup>1</sup> and Yasushi SUTO<sup>2,3</sup>

<sup>1</sup>Department of Physics, Tokyo Metropolitan University, Hachioji, Tokyo 192-0397, Japan

<sup>2</sup>Department of Physics, The University of Tokyo, Tokyo 113-0033, Japan

<sup>3</sup>Research Center for the Early Universe, School of Science, The University of Tokyo, Tokyo 113-0033, Japan

\*E-mail: sasaki@phys.se.tmu.ac.jp

Received 2021 July 29; Accepted

## Abstract

The Rossiter-McLaughlin (RM) effect has been widely used to estimate the *sky-projected* spin-orbit angle,  $\lambda$ , of transiting planetary systems. Most of the previous analysis assume that the host stars are rigid rotators in which the amplitude of the RM velocity anomaly is proportional to  $v_* \sin i_*$ . When their latitudinal differential rotation is taken into account, one can break the degeneracy, and determine separately the equatorial rotation velocity  $v_*$  and the inclination  $i_*$  of the host star. We derive a fully analytic approximate formula for the RM effect adopting a parameterized model for the stellar differential rotation. For those stars that exhibit the differential rotation similar to that of the Sun, the corresponding RM velocity modulation amounts to several m/s. We conclude that the latitudinal differential rotation offers a method to estimate  $i_*$ , and thus the full spin-orbit angle  $\psi$ , from the RM data analysis alone.

**Key words:** planetary systems — planets and satellites: formation — planets and satellites: general —

## 1 Introduction

The spin-orbit angle  $\psi$  of planetary systems is a unique probe of their origin and evolution. Observationally,  $\psi$  can be estimated for transiting planetary systems from the inclination angle of the planetary orbit,  $i_{\text{orb}}$ , the projected spin-orbit angle,  $\lambda$ , and the stellar inclination,  $i_{\star}$ , as

$$\cos \psi = \sin i_{\star} \sin i_{\text{orb}} \cos \lambda + \cos i_{\star} \cos i_{\text{orb}}. \quad (1)$$

For the transiting planets,  $i_{\text{orb}} \approx \pi/2$ , and equation (1) is approximately given as

$$\cos \psi \approx \sin i_{\star} \cos \lambda. \quad (2)$$

Thus either  $\sin i_{\star} \ll 1$  or  $\cos \lambda \ll 1$  is a necessary condition for the significant spin-orbit misalignment  $\cos \psi \ll 1$ .

For isolated and stable systems like our Solar system,  $\psi$  is supposed to keep the initial value at the formation epoch. For instance, in the simplest scenario, the star and the surrounding protoplanetary disk are likely to share the same direction of the angular momentum of the progenitor molecular cloud (Takaishi et al. 2020). Therefore planets formed in the disk are expected to have  $\psi \sim 0$ , as is the case for all the eight solar planets ( $\psi < 6^\circ$ ).

Such a naive expectation, however, is not necessarily the case for the observed distribution of  $\lambda$  (Xue et al. 2014; Winn & Fabrycky 2015); more than 20 percents of transiting close-in gas-giant planets are misaligned, in the sense that the  $2\sigma$  lower limit of their measured  $\lambda$  exceeds  $30^\circ$  (Kamiaka et al. 2019). While the origin of such a misalignment is not yet well understood, possible scenarios include planetary migration (Lin et al. 1996), planet-planet scattering (Rasio & Ford 1996; Nagasawa et al. 2008; Nagasawa & Ida 2011), and perturbation due to distant outer objects (e.g., Kozai 1962; Lidov 1962; Fabrycky & Tremaine 2007; Batygin 2012; Xue et al. 2014, 2017).

We would like to stress that spin-orbit misaligned systems are often defined by the value of  $\lambda$  alone that are measured from the Rossiter-McLaughlin (RM) effect, which is the radial velocity anomaly of the host star due to a distortion of the stellar line profiles during the planetary transit (e.g., Rossiter 1924; McLaughlin 1924; Ohta et al. 2005; Winn et al. 2005).

On the other hand, the stellar inclination may be inferred either from asteroseismology (e.g., Gizon & Solanki 2003) or from the combination of the estimated stellar radius  $R_{\star}$ ,

spectroscopically measured ( $v_\star \sin i_\star$ ), and photometric stellar rotation period  $P_\star$ :

$$\sin i_\star = \frac{(v_\star \sin i_\star) P_\star}{2\pi R_\star}. \quad (3)$$

The above two methods, however, do not always agree with each other, and the reliable estimate has been made only to a limited number of systems (Kamiaka et al. 2018, 2019).

While  $\lambda$  has been measured for more than 150 transiting systems<sup>1</sup>,  $i_\star$  are available from asteroseismology only for a couple of systems, Kepler-25c and HAT-P-7 (Benomar et al. 2014), and about thirty systems have  $i_\star$  estimated spectroscopically from equation (3); see Hirano et al. (2012) for instance. More recently, Louden et al. (2021) derived a statistical distribution of  $\langle \sin i_\star \rangle$  for a sample of 150 Kepler stars with transiting planets smaller than Neptune. Therefore, a complementary method to estimate  $i_\star$  breaking the degeneracy in  $v_\star \sin i_\star$  is essential to understand the distribution of the spin-orbit angle  $\psi$  (c.f., Albrecht et al. 2021).

The RM effect of transiting planets was measured by Queloz et al. (2000) for the first time. Ohta et al. (2005) derived an analytic approximate formula for the RM effect, which were improved later by Hirano et al. (2010) and Hirano et al. (2011b). Such analytic expressions for the RM effect are useful in understanding the parameter dependence and degeneracy that are not easy to extract from numerical analysis. Furthermore, Hirano et al. (2011b) and Hirano et al. (2011a) attempted to examine the effect of the differential rotation for the rapidly rotating XO-3 system ( $v_\star \sin i_\star \approx 18\text{m/s}$  and  $\lambda \approx 40^\circ$ ), but their result was not so constraining mainly due to the large stellar jitter for such host stars ( $\sim 15\text{m/s}$ ).

In the present paper, we improved the previous model for the RM effect incorporating the differential rotation of the host star. Since our model is fully analytic, one clearly understand how  $i_\star$  and  $\lambda$  can be inferred from the RM modulation due to the differential rotation; see equation (30) below. We find that the differential rotation similar to the Sun produces an additional feature of an amplitude on the order of several m/s in the RM effect, which should be detectable for systems with good signal-to-noise ratios. Thus our analytic formula is useful in breaking the degeneracy of  $v_\star \sin i_\star$ , and allows the determination of  $i_\star$ , and thus the true spin-orbit angle  $\psi$ , for transiting planetary systems with the differential rotation of the host stars.

## 2 Coordinates of the star and the transiting planet in the observer's frame

We introduce three coordinate systems for the present analysis, whose origin is chosen as the center of the host star. The observer's frame (O-frame) is represented by  $(X, Y, Z)$ . The Z-axis

<sup>1</sup> <https://www.astro.keele.ac.uk/jkt/tepcat/obliquity.html>

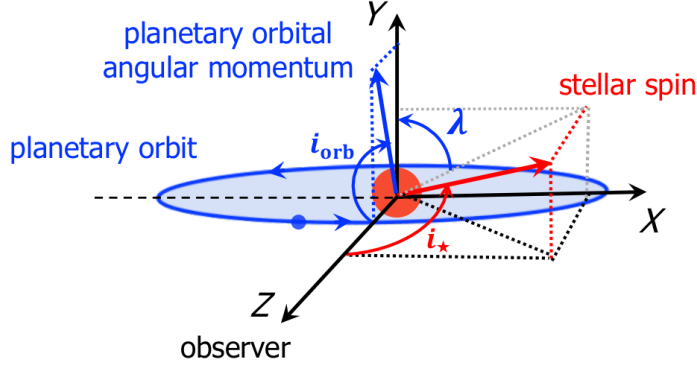


**Fig. 1.** Spin-orbit architecture of transiting planetary systems in the observer's frame (O-frame);  $i_*$  and  $i_{\text{orb}}$  are the stellar inclination and the planetary orbital inclination with respect to the observer, while  $\lambda$  is the sky-projected spin-orbit angle.

is directed toward the observer, and the Y-axis is chosen in such a way that the orbital angular momentum vector of the planet lies on the YZ plane (Figure 1).

The planetary frame (P-frame) is represented by  $(\tilde{x}, \tilde{y}, \tilde{z})$ . The planetary orbit is on the  $\tilde{x}\tilde{y}$  plane, thus the  $\tilde{z}$ -axis is along the direction of the orbital angular momentum vector of the planet (Figure 2). Finally, the stellar frame (S-frame) is represented by  $(x, y, z)$ , and the  $z$ -axis is chosen as the direction of the stellar spin vector.

An arbitrary vector  $\mathbf{A}$  defined in the O-frame is related to  $\tilde{\mathbf{a}}$  in the P-frame as

$$\begin{pmatrix} A_1 \\ A_2 \\ A_3 \end{pmatrix} = R_3(\Omega)R_1(i_{\text{orb}})R_3(\omega) \begin{pmatrix} \tilde{a}_1 \\ \tilde{a}_2 \\ \tilde{a}_3 \end{pmatrix}, \quad (4)$$

where  $R_i(\theta)$  denote the rotation matrix by angle  $\theta$  around the  $i$ -th axis, and  $i_{\text{orb}}$ ,  $\Omega$ ,  $\omega$  are the orbital inclination, the longitude of the ascending node, and the argument of pericenter of the planet, respectively (Figure 2).

Similarly,  $\mathbf{A}$  in the O-frame is related to  $\mathbf{a}$  in the S-frame:

$$\begin{pmatrix} A_1 \\ A_2 \\ A_3 \end{pmatrix} = R_3(-\lambda)R_1(-i_*)R_3(\phi) \begin{pmatrix} a_1 \\ a_2 \\ a_3 \end{pmatrix}, \quad (5)$$

where  $i_*$  and  $\lambda$  denote the stellar inclination and the projected spin-orbit angle, and  $\phi$  is the azimuthal angle. We consider axi-symmetric stars in this paper, thus hereafter we fix  $\phi = 0$  without loss of generality.

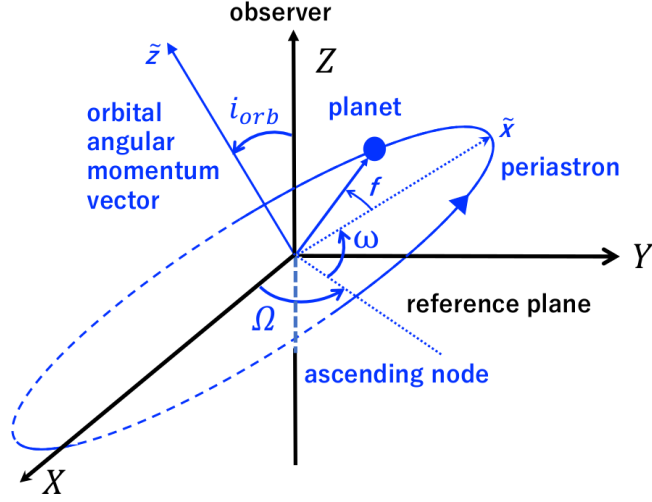


Fig. 2. Planetary orbit in the observer's frame  $(X, Y, Z)$  and in the planetary frame  $(\tilde{x}, \tilde{y}, \tilde{z})$ .

### 3 Radial component of the stellar surface rotation velocity at the projected position of the transiting planet

The position vector of a planet in the P-frame is expressed as

$$\begin{pmatrix} \tilde{x}_p \\ \tilde{y}_p \\ \tilde{z}_p \end{pmatrix} = \frac{a(1-e^2)}{1+e\cos f} \begin{pmatrix} \cos f \\ \sin f \\ 0 \end{pmatrix}, \quad (6)$$

where  $a$  and  $e$  are the semi-major axis and eccentricity of the planetary orbit, and  $f$  is the true anomaly. Equation (6) is transformed to that in the O-frame using equation (4):

$$\begin{pmatrix} X_p \\ Y_p \\ Z_p \end{pmatrix} = \frac{a(1-e^2)}{1+e\cos f} \begin{pmatrix} -\sin\Omega \sin(f+\omega) \cos i_{orb} + \cos\Omega \cos(f+\omega) \\ \sin\Omega \cos(f+\omega) + \sin(f+\omega) \cos i_{orb} \cos\Omega \\ \sin i_{orb} \sin(f+\omega) \end{pmatrix}. \quad (7)$$

Essentially, the RM effect measures the line-of-sight component of the stellar surface velocity at the projected surface position  $(x_{sp}, y_{sp}, z_{sp})$  in the S-frame that corresponds to  $(X_p, Y_p, Z_p)$  in the O-frame as the planet transits over the stellar surface. So we first project  $(X_p, Y_p, Z_p)$  in the O-frame on the position on the stellar surface:

$$\begin{pmatrix} X_{sp} \\ Y_{sp} \\ Z_{sp} \end{pmatrix} = \begin{pmatrix} X_p \\ Y_p \\ \sqrt{R_\star^2 - X_p^2 - Y_p^2} \end{pmatrix}, \quad (8)$$

where

$$Z_{sp} = \frac{a(1-e^2)}{1+e\cos f} \sqrt{\frac{R_\star^2(1+e\cos f)^2}{a^2(1-e^2)^2} - [\sin^2(f+\omega) \cos^2 i_{orb} + \cos^2(f+\omega)]}. \quad (9)$$

Next, we rotate  $(X_{sp}, Y_{sp}, Z_{sp})$  to that in the S-frame using equation (5):

$$\begin{aligned} \begin{pmatrix} x_{sp} \\ y_{sp} \\ z_{sp} \end{pmatrix} &= R_1(+i_\star)R_3(+\lambda) \begin{pmatrix} X_{sp} \\ Y_{sp} \\ Z_{sp} \end{pmatrix} \\ &= \begin{pmatrix} 1 & 0 & 0 \\ 0 & \cos i_\star & -\sin i_\star \\ 0 & \sin i_\star & \cos i_\star \end{pmatrix} \begin{pmatrix} \cos \lambda & -\sin \lambda & 0 \\ \sin \lambda & \cos \lambda & 0 \\ 0 & 0 & 1 \end{pmatrix} \begin{pmatrix} X_p \\ Y_p \\ Z_{sp} \end{pmatrix}. \end{aligned} \quad (10)$$

Specifically, we obtain the planetary position in the S-frame in terms of the orbital elements:

$$x_{sp} = \frac{a(1-e^2)}{1+e\cos f} \left[ \cos(\lambda + \Omega) \cos(f + \omega) - \cos i_{\text{orb}} \sin(\lambda + \Omega) \sin(f + \omega) \right], \quad (11)$$

$$y_{sp} = \frac{a(1-e^2)}{1+e\cos f} \left[ \cos i_\star (\sin(\lambda + \Omega) \cos(f + \omega) + \cos(\lambda + \Omega) \cos i_{\text{orb}} \sin(f + \omega)) - \sin i_\star Z_{sp} \right], \quad (12)$$

$$z_{sp} = \frac{a(1-e^2)}{1+e\cos f} \sin i_\star \left[ \sin(\lambda + \Omega) \cos(f + \omega) + \cos(\lambda + \Omega) \cos i_{\text{orb}} \sin(f + \omega) \right] + \cos i_\star Z_{sp}. \quad (13)$$

Consider a point on the stellar surface at latitude  $\ell$  and longitude  $\varphi$  in the S-frame:

$$\begin{pmatrix} x \\ y \\ z \end{pmatrix} = R_\star \begin{pmatrix} \cos \ell \cos \varphi \\ \cos \ell \sin \varphi \\ \sin \ell \end{pmatrix}. \quad (14)$$

If the stellar surface rotates around the  $z$ -axis, the corresponding velocity in the S-frame is given by

$$\begin{pmatrix} v_x \\ v_y \\ v_z \end{pmatrix} = R_\star \dot{\varphi}(\ell) \begin{pmatrix} -\cos \ell \sin \varphi \\ \cos \ell \cos \varphi \\ 0 \end{pmatrix} = \dot{\varphi}(\ell) \begin{pmatrix} -y \\ x \\ 0 \end{pmatrix}. \quad (15)$$

In what follows, we adopt the following parameterized model for the latitudinal differential rotation:

$$\dot{\varphi}(\ell) = \omega_0(1 - \alpha_2 \sin^2 \ell - \alpha_4 \sin^4 \ell). \quad (16)$$

For the Sun,  $\omega_{0\odot} \approx 2.972 \times 10^{-6} \text{ rad s}^{-1}$ ,  $\alpha_{2\odot} \approx 0.163$ , and  $\alpha_{4\odot} \approx 0.121$  (Snodgrass & Ulrich 1990). The differential rotation of stars is not so accurately measured except for the Sun. Brun et al. (2017) presented a model from their numerical simulations in which the amplitude of the latitudinal differential rotation changes by about 20 percent, roughly consistent with the Sun. It is not clear, however, to what extent the result is applicable for other stars.

The stellar surface velocity (15) in the S-frame is transformed into that in the O-frame

using equation (5):

$$\begin{pmatrix} V_X \\ V_Y \\ V_Z \end{pmatrix} = R_3(-\lambda)R_1(-i_\star) \begin{pmatrix} v_x \\ v_y \\ v_z \end{pmatrix} = \dot{\varphi}(\ell) \begin{pmatrix} -y \cos \lambda + x \sin \lambda \cos i_\star \\ y \sin \lambda + x \cos i_\star \cos \lambda \\ -x \sin i_\star \end{pmatrix}. \quad (17)$$

Finally, equations (11) and (17) yield

$$\begin{aligned} V_Z(\mathbf{r}_{sp}) &= -x_{sp} \dot{\varphi}(\ell) \sin i_\star \\ &= \frac{a(1-e^2)}{1+e \cos f} \dot{\varphi}(\ell) \sin i_\star [\cos i_{\text{orb}} \sin(\lambda + \Omega) \sin(f + \omega) - \cos(\lambda + \Omega) \cos(f + \omega)], \end{aligned} \quad (18)$$

where the latitude  $\ell$  is computed from equations (13) and (14)

$$\begin{aligned} \frac{R_\star(1+e \cos f)}{a(1-e^2)} \sin \ell &= \sin i_\star (\sin(\lambda + \Omega) \cos(f + \omega) + \cos(\lambda + \Omega) \cos i_{\text{orb}} \sin(f + \omega)) \\ &\quad + \cos i_\star \sqrt{\frac{R_\star^2(1+e \cos f)^2}{a^2(1-e^2)^2} - [\cos^2 i_{\text{orb}} \sin^2(f + \omega) + \cos^2(f + \omega)]}. \end{aligned} \quad (19)$$

#### 4 Differential rotation effect for a circular planetary orbit

Equation (18) with equation (19) provides the key result that disentangles  $i_\star$  through the differential rotation of the host stars using the RM effect alone. For definiteness, we focus on a circular orbit ( $e = 0$ ,  $\omega = 0$  and  $\Omega = \pi$ ) in this section. Then, equation (19) is simplified as

$$\begin{aligned} \frac{R_\star}{a} \sin \ell &= \cos i_\star \sqrt{\frac{R_\star^2}{a^2} - (\cos^2 i_{\text{orb}} \sin^2 f + \cos^2 f)} \\ &\quad - \sin i_\star (\sin \lambda \cos f + \cos \lambda \cos i_{\text{orb}} \sin f). \end{aligned} \quad (20)$$

Since  $(X_p, Y_p) \approx (-a \cos f, -a \cos i_{\text{orb}})$ , the true anomaly during the transit ( $X_p^2 + Y_p^2 < R_\star^2$ ) may be approximated as

$$f \equiv \frac{\pi}{2} + \Delta f, \quad (21)$$

where

$$-\sqrt{\left(\frac{R_\star}{a}\right)^2 - \cos^2 i_{\text{orb}}} < \Delta f < \sqrt{\left(\frac{R_\star}{a}\right)^2 - \cos^2 i_{\text{orb}}}. \quad (22)$$

We define the dimensionless impact parameter  $b$  and dimensionless time variable  $\tau$ :

$$\cos i_{\text{orb}} \equiv \frac{R_\star}{a} b \quad (0 < b < 1), \quad (23)$$

$$\Delta f \equiv \frac{R_\star \sqrt{1-b^2}}{a} \tau \quad (-1 < \tau < 1). \quad (24)$$

Thus equation (20) reduces to

$$\sin \ell \approx \cos i_\star \sqrt{1-b^2} \sqrt{1-\tau^2} - \sin i_\star \left( \tau \sqrt{1-b^2} \sin \lambda + b \cos \lambda \right). \quad (25)$$

Equation (18) with equation (16) reduces to

$$\begin{aligned} V_Z(\tau) &\approx R_* \omega_0 \sin i_* (1 - \alpha_2 \sin^2 \ell - \alpha_4 \sin^4 \ell) \left( \tau \sqrt{1 - b^2} \cos \lambda + b \sin \lambda \right) \\ &\equiv V_{\text{rigid}}(\tau) + V_{\text{diff}}(\tau), \end{aligned} \quad (26)$$

where the rigid rotation component is

$$V_{\text{rigid}}(\tau) \equiv v_* \sin i_* \left( \tau \sqrt{1 - b^2} \cos \lambda + b \sin \lambda \right), \quad (27)$$

and the additional modulation term due to the differential rotation is

$$\begin{aligned} V_{\text{diff}}(\tau) &\equiv -(\alpha_2 \sin^2 \ell + \alpha_4 \sin^4 \ell) V_{\text{rigid}} \\ &= - \left\{ \alpha_2 \left[ \cos i_* \sqrt{1 - b^2} \sqrt{1 - \tau^2} - \sin i_* \left( \tau \sqrt{1 - b^2} \sin \lambda + b \cos \lambda \right) \right]^2 \right. \\ &\quad \left. + \alpha_4 \left[ \cos i_* \sqrt{1 - b^2} \sqrt{1 - \tau^2} - \sin i_* \left( \tau \sqrt{1 - b^2} \sin \lambda + b \cos \lambda \right) \right]^4 \right\} \\ &\quad \times v_* \sin i_* \left( \tau \sqrt{1 - b^2} \cos \lambda + b \sin \lambda \right). \end{aligned} \quad (28)$$

If we assume a rigid rotation for the central star, time-variation of equation (27) is specified by  $v_* \sin i_*$  and  $\lambda$  (the impact parameter  $b$  is estimated from the transit lightcurve). The differential rotation term, equation (28), can break the degeneracy of  $v_* \sin i_*$ , and enables us to estimate  $\alpha_2$ ,  $\alpha_4$  and  $i_*$  separately in principle, through, for instance, the measurements at the central transit ( $\tau = 0$ ) and egress/ingress ( $\tau = \pm 1$ ) phases:

$$\begin{aligned} \frac{V_{\text{diff}}(0)}{v_* \sin i_*} &= -b \sin \lambda (b \sin i_* \cos \lambda - \sqrt{1 - b^2} \cos i_*)^2 \\ &\quad \times [\alpha_2 + \alpha_4 (b \sin i_* \cos \lambda - \sqrt{1 - b^2} \cos i_*)^2], \end{aligned} \quad (29)$$

$$\begin{aligned} \frac{V_{\text{diff}}(\pm 1)}{v_* \sin i_*} &= -\sin^2 i_* (b \cos \lambda \pm \sqrt{1 - b^2} \sin \lambda)^2 (b \sin \lambda \pm \sqrt{1 - b^2} \cos \lambda) \\ &\quad \times [\alpha_2 + \alpha_4 \sin^2 i_* (b \cos \lambda \pm \sqrt{1 - b^2} \sin \lambda)^2]. \end{aligned} \quad (30)$$

Strictly speaking, however, the RM effect does not measure directly  $V_Z(\mathbf{r}_{sp})$ , but its convolution over the stellar disk including the limb darkening, which will be taken into account in the next section.

## 5 Analytic approximation to the Rossiter-McLaughlin effect for differentially rotating stars

### 5.1 The Rossiter-McLaughlin effect in Gaussian approximation

The RM radial velocity anomaly  $\Delta v_{\text{RM}}$  is roughly given by

$$\Delta v_{\text{RM}} = -\frac{f}{1 - f} v_p, \quad (31)$$

where  $v_p$  is the line-of-sight velocity of the stellar surface element occulted by the planet, and  $f (\ll 1)$  represents the fraction of the occulted area in units of the stellar disk area (Ohta et al.



2005). Equation (31) does not take into account the stellar line profile due to the thermal and rotational broadenings, and micro/macro-turbulences.

Hirano et al. (2010) and Hirano et al. (2011b) improved equation (31), and derived the following analytic formula under the Gaussian line profile approximation:

$$\Delta v_{\text{RM}} = - \left( \frac{2\beta_{\star}^2}{\beta_{\star}^2 + \beta_p^2} \right)^{3/2} f v_p \exp \left( - \frac{v_p^2}{\beta_{\star}^2 + \beta_p^2} \right), \quad (32)$$

where

$$\beta_p^2 = \beta^2 + \zeta^2, \quad (33)$$

$$\beta_{\star}^2 = \beta^2 + \zeta^2 + \sigma_{\star}^2, \quad (34)$$

$$\sigma_{\star}^2 \approx (v_{\star} \sin i_{\star} / 1.3)^2. \quad (35)$$

In the above expressions,  $\beta$  represents the thermal broadening and micro-turbulence due to the convection, and  $\zeta$  corresponds to macroturbulence that may be approximated as

$$\zeta \approx \left( 3.98 + \frac{T_{\text{eff}} - 5770\text{K}}{650\text{K}} \right) \text{ km/s} \quad (36)$$

(Valenti & Fischer 2005; Hirano et al. 2012).

The stellar lines are additionally broadened by the stellar rotation, whose Gaussian width is found to be approximated as equation (35) by Hirano et al. (2010). Note that Hirano et al. (2010) and Hirano et al. (2011b) adopted the Gaussian profile  $\propto e^{-x^2/\sigma^2}$  instead of  $\propto e^{-x^2/2\sigma^2}$ . Thus equations (32) to (35) are slightly different from equation (2) in Boué et al. (2013), for instance.

The fraction of the occulted area neglecting the limb darkening can be computed from equations (B1) to (B3) in Hirano et al. (2010). Figure 3 shows relevant angles in the O-frame in which the centers of the star and planet are located at  $(X, Y) = (0, 0)$  and  $(X_p, Y_p)$  given by equation (10):

$$\cos \Delta\varphi_{\star} = \frac{R_{\star}^2 + R^2 - R_p^2}{2R_{\star}R}, \quad (37)$$

$$\cos \Delta\varphi_p = \frac{R_p^2 + R^2 - R_{\star}^2}{2R_pR}, \quad (38)$$

$$R = \sqrt{X_p^2 + Y_p^2}, \quad (39)$$

with  $R_p$  being the radius of the planet. Then the fraction  $f_0(R)$  neglecting limb darkening is given as

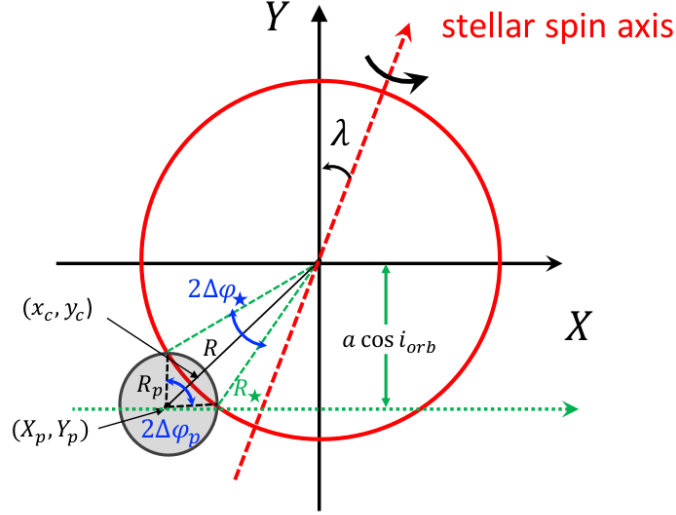


Fig. 3. Schematic illustration of the stellar disk occulted by a transiting planet at the ingress/egress phases.

$$f_0(R) = \begin{cases} 0 & (R > R_* + R_p) \\ \frac{1}{\pi} \left[ \Delta\varphi_* - \frac{\sin 2\Delta\varphi_*}{2} + \frac{R_p^2}{R_*^2} \left( \Delta\varphi_p - \frac{\sin 2\Delta\varphi_p}{2} \right) \right] & (R_* - R_p \leq R \leq R_* + R_p) \\ \frac{R_p^2}{R_*^2} & (R < R_* - R_p) \end{cases} \quad (40)$$

## 5.2 Effect of Limb-darkening

We adopt the quadratic limb darkening law in the S-frame:

$$f_{LD}(x, y) = \frac{I(x, y)}{I(0, 0)} = 1 - 2q_2\sqrt{q_1}(1 - \mu) - \sqrt{q_1}(1 - 2q_2)(1 - \mu)^2, \quad (41)$$

$$\mu = \sqrt{1 - \frac{x^2 + y^2}{R_*^2}}, \quad (42)$$

where  $I(x, y)$  is the stellar intensity at a location  $(x, y)$  (Kipping 2013). The parameters  $q_1$  and  $q_2$  are related to  $u_1, u_2$  which are used in Hirano et al. (2010) by the following equation:

$$q_1 = (u_1 + u_2)^2, \quad q_2 = \frac{u_1}{2(u_1 + u_2)}. \quad (43)$$

We approximate the effect of the limb darkening of the occulted region by the value evaluated at  $(x_c, y_c)$ , instead of integrating over the corresponding area:

$$\begin{pmatrix} x_c \\ y_c \end{pmatrix} = \begin{cases} \frac{R_* + R - R_p}{2r} \begin{pmatrix} X_p \\ Y_p \end{pmatrix} & (R_* - R_p \leq R \leq R_* + R_p) \\ \begin{pmatrix} X_p \\ Y_p \end{pmatrix} & (R < R_* - R_p) \end{cases} \quad (44)$$

**Table 1.** Adopted parameters for the system considered in section 6.

Name	Symbol	Fiducial Value	reference
star			
radius	$R_\star$	$1.14R_\odot$	Casasayas-Barris et al. (2021)
spin velocity	$v_\star \sin i_\star$	4.5 km/s	Hirano et al. (2011b)
Gaussian fitting	$\beta$	4.0 km/s	Hirano et al. (2011b)
	$\zeta$	4.3 km/s	Hirano et al. (2011b)
	$\sigma_\star$	$\frac{v_\star \sin i_\star}{1.3}$	Hirano et al. (2011b)
limb darkening	$(q_1, q_2)$	(0.56, 0.32)	Hirano et al. (2010)
differential rotation	$(\alpha_2, \alpha_4)$	(0.163, 0.121)	Snodgrass & Ulrich (1990) Solar value
planet			
radius ratio	$R_p/R_\star$	0.121	Casasayas-Barris et al. (2021)
orbit			
orbital period	$P_{\text{orb}}$	3.5 days	Casasayas-Barris et al. (2021)
semi-major axis	$a$	0.047 au	Casasayas-Barris et al. (2021)

We adopt fiducial values of parameters mainly from the HD209458 system except for  $i_{\text{orb}}$ ,  $i_\star$ ,  $\lambda$ , and the differential rotation parameters  $(\alpha_2, \alpha_4)$ . For simplicity, we consider a circular orbit ( $e = 0$ ), and thus fix  $\omega = 0$  and  $\Omega = \pi$  without loss of generality.

Thus we use

$$f(R) \approx f_{\text{LD}}(x_c, y_c) f_0(X_p, Y_p) \left[ 1 - \frac{2\sqrt{q_1}q_2}{3} - \frac{\sqrt{q_1}(1-2q_2)}{6} \right]^{-1}. \quad (45)$$

Also we adopt equation (18) evaluated at  $(x_c, y_c)$  for  $v_p$  in equation (32):

$$v_p(\mathbf{r}_{sp}) = V_Z(x_c, y_c). \quad (46)$$

## 6 Results

Equation (32) with equations (45) and (46) provides an analytic formula for the RM velocity anomaly taking account of the differential rotation of the host star.

In order to examine to what extent one can break the degeneracy of  $i_\star$  using the differential rotation, we assume a set of fiducial values for system parameters (Table 1). They are adopted from the HD209458 system, except for  $i_{\text{orb}}$ ,  $i_\star$ ,  $\lambda$ , and the differential rotation parameters  $(\alpha_2, \alpha_4)$ , which we vary in the analysis below. For simplicity, we consider a circular orbit and fix  $\omega = 0$  and  $\Omega = \pi$ . Since we fix the equatorial stellar velocity  $v_\star \sin i_\star = 4.5 \text{ km/s}$ , the equatorial angular velocity is assumed to vary as  $\sin i_\star$  as

$$\omega_0 = \frac{4.5 \text{ km/s}}{R_\star \sin i_\star}. \quad (47)$$

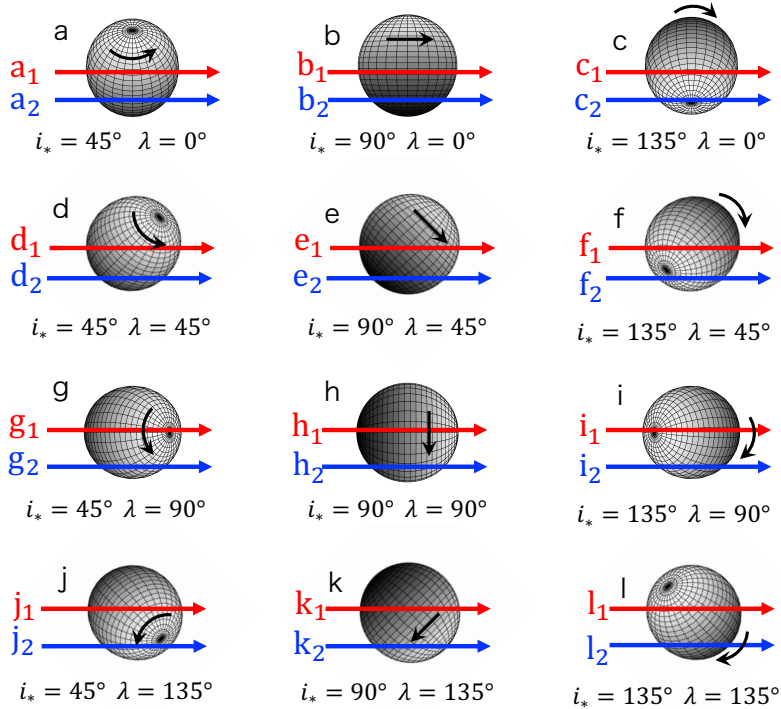


**Fig. 4.** Schematic trajectories of transiting planets on the stellar disk for different  $i_*$  and  $\lambda$ . Upper and lower arrows in each panel illustrate trajectories for  $i_{\text{orb}} = 90^\circ (b = 0)$  and  $i_{\text{orb}} < 90^\circ (b \neq 0)$ .

### 6.1 Dependence on the differential rotation parameters

Figure 4 illustrates schematic trajectories of planets during their transits for different combinations of the spin-orbit angles ( $i_*, \lambda$ ). The corresponding RM velocity anomaly  $\Delta v_{\text{RM}}$  for each panel is plotted in Figures 5 and 6 for  $i_{\text{orb}} = 90^\circ (b = 0)$  and  $87^\circ (b \approx 0.47)$ , respectively, for different combinations of  $\alpha_2$  and  $\alpha_4$ .

First, let us consider panels a to c in Figure 5, in which  $i_{\text{orb}} = 90^\circ$  and  $\lambda = 0$ . Since planets in panels a and c move away from the stellar equator (Figure 4), the corresponding  $\Delta v_{\text{RM}}(t)$  with differential rotation becomes smaller than that for rigid rotator. Due to the symmetry between  $l \leftrightarrow -l$  in equation (16),  $\Delta v_{\text{RM}}(t)$  in panels a and c is identical. In contrast, panel b corresponds to the planetary trajectory along the equator (Figure 4),  $\Delta v_{\text{RM}}(t)$  is not affected by the presence of differential rotation.

Similarly, one may understand the behavior of panels d to f ( $\lambda = 45^\circ$ ) by comparing with the corresponding trajectories in Figure 4. Since the trajectory  $d_1$  moves from low to high latitude regions, the effect of differential rotation is stronger after the central transit epoch as shown in Figure 5. The trajectory  $f_1$  is opposite, and the trajectory  $e_1$  corresponds to the case

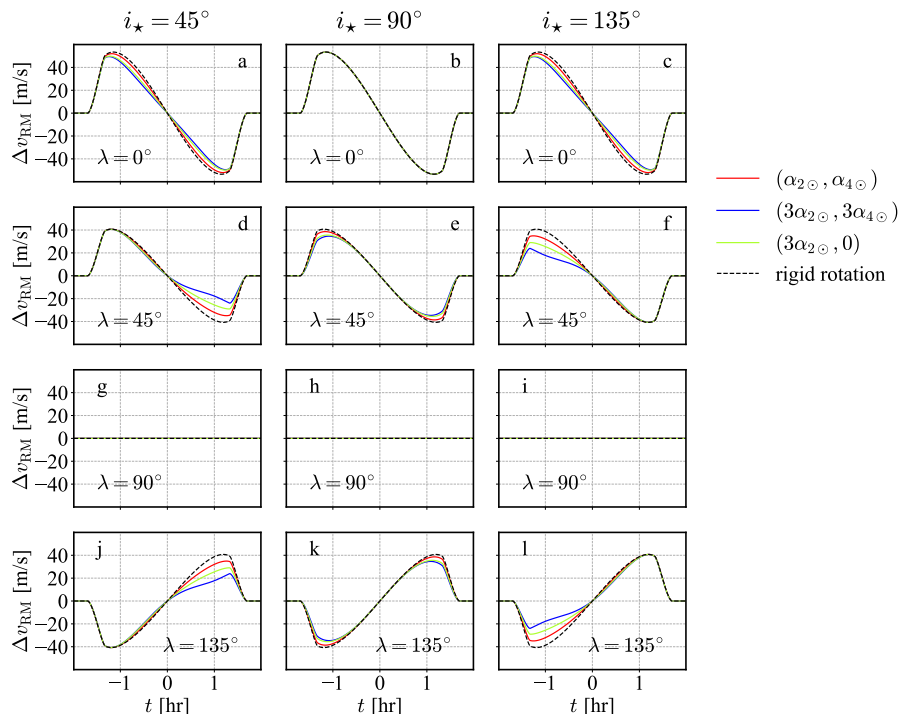


**Fig. 5.** Effect of the stellar latitudinal differential rotation on the RM velocity anomaly  $\Delta v_{\text{RM}}(t)$  for  $i_{\text{orb}} = 90^\circ$  ( $b = 0$ ) for different values of  $\lambda$  and  $i_*$ . Each panel corresponds to the upper trajectories shown in Figure 4. Red, blue, and greenyellow curves are for  $(\alpha_2, \alpha_4) = (\alpha_{2\odot}, \alpha_{4\odot})$ ,  $(3\alpha_{2\odot}, 3\alpha_{4\odot})$ , and  $(3\alpha_{2\odot}, 0)$ , respectively. Dashed curves indicate the case for rigid rotation ( $\alpha_2 = \alpha_4 = 0$ ). We do not plot the case for  $(\alpha_2, \alpha_4) = (0, 3\alpha_{4\odot})$  because it is very close to models with  $(\alpha_2, \alpha_4) = (\alpha_{2\odot}, \alpha_{4\odot})$ .

between the two cases.

Panels j to l ( $\lambda = 135^\circ$ ) are easily understood from panels d to f since equations (18) and (19) indicates  $V_z(\lambda) = -V_z(\pi - \lambda)$  for  $i_{\text{orb}} = 90^\circ$ . Finally, panels g to i ( $\lambda = 90^\circ$ ) correspond to the trajectories with  $V_z = 0$  for  $i_{\text{orb}} = 90^\circ$ .

Consider next the case for  $i_{\text{orb}} = 87^\circ$  ( $b \approx 0.47$ ), *i.e.*, Figure 6 and lower trajectories in the corresponding panels of Figure 4. In this case, the symmetry between  $\lambda \leftrightarrow \pi - \lambda$  no longer holds, and  $\Delta v_{\text{RM}}(t)$  exhibits small but clear dependence on  $i_{\text{orb}}$ ,  $i_*$ , and  $\lambda$ .

In conclusion, Figures 5 and 6 imply that the differential rotation can be used to estimate  $i_*$  from the RM velocity anomaly curve through the latitudinal dependence of  $\dot{\varphi}(\ell)$  in equations (18) and (19).

## 6.2 Sensitivity to the stellar inclination

Figure 7 compares  $\Delta v_{\text{RM}}$  with and without differential rotation for different values of  $(i_{\text{orb}}, \lambda)$ . Figure 8 plots the corresponding RM modulation term due to the differential rotation alone,  $\Delta v_{\text{RM}}(i_*) - \Delta v_{\text{RM}}(\text{rigid rotation})$ . In most cases, the amplitude of the modulation term becomes

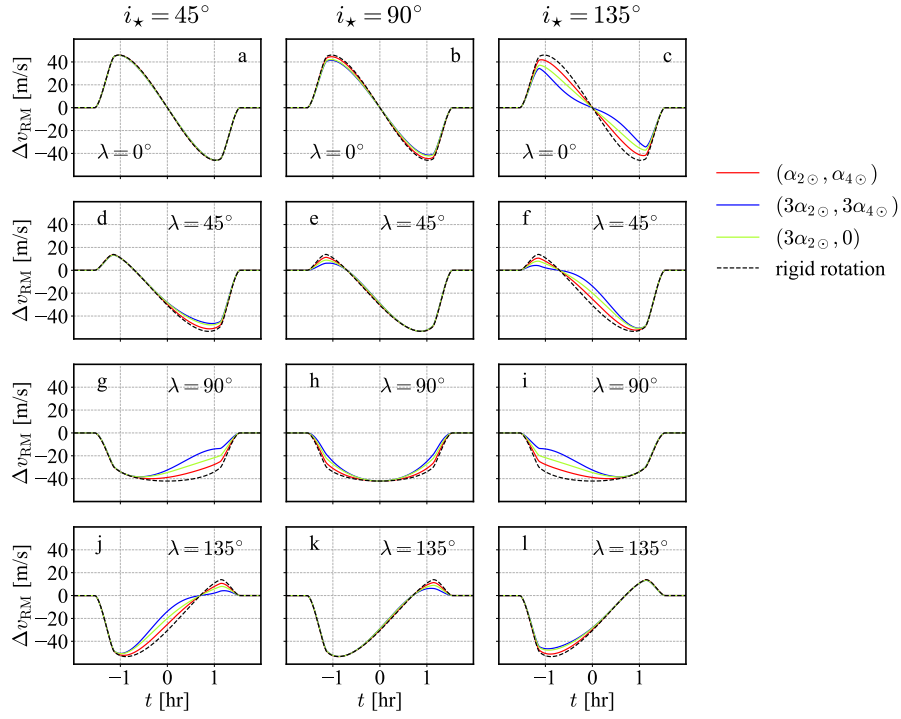


Fig. 6. Same as Figure 5 except for  $i_{\text{orb}} = 87^\circ$  ( $b \approx 0.47$ ).

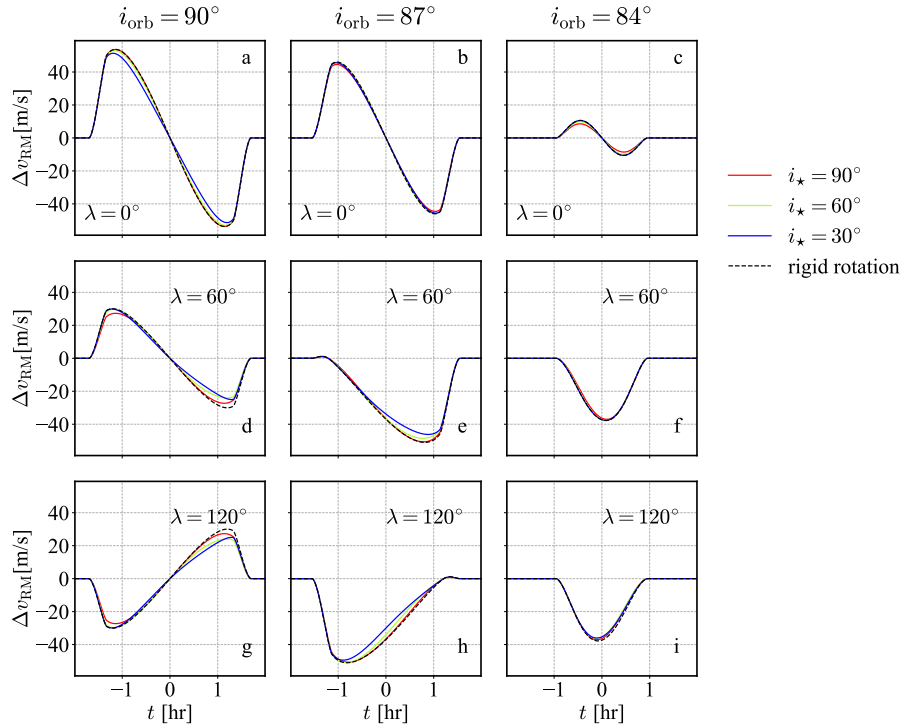
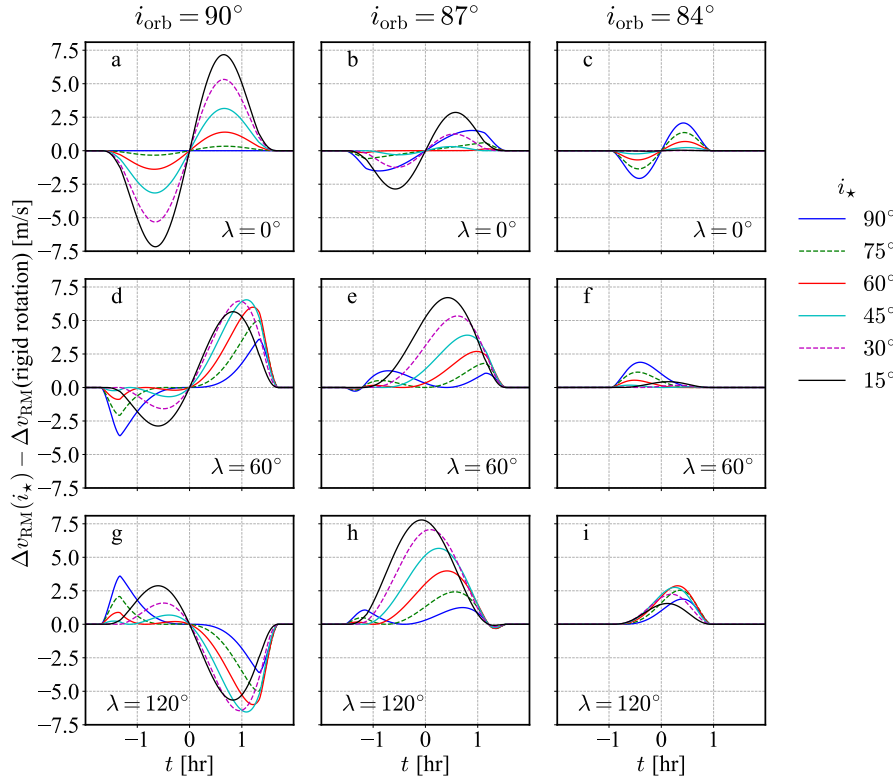


Fig. 7. Dependence of  $\Delta v_{\text{RM}}$  on the stellar inclination  $i_*$ , where the equatorial velocity  $v_* \sin i_*$  is fixed (4.5 km/s). Dashed lines correspond to the rigid rotation model. Left, middle, and right panels correspond to  $i_{\text{orb}} = 90^\circ$  ( $b = 0$ ),  $87^\circ$  ( $b \approx 0.47$ ), and  $84^\circ$  ( $b \approx 0.93$ ). Red, greenyellow, and blue curves indicate  $i_* = 90^\circ$ ,  $60^\circ$ , and  $30^\circ$ , respectively, for the differential rotation model with  $\alpha_2 = \alpha_{2\odot}$  and  $\alpha_4 = \alpha_{4\odot}$ .



**Fig. 8.** The RM modulation term due to the differential rotation after subtracting the rigid rotation component. Each panel adopts the values of  $\lambda$  and  $i_{\text{orb}}$  in the corresponding panel of Figure 7. We adopt  $\alpha_2 = \alpha_{2\odot}$  and  $\alpha_4 = \alpha_{4\odot}$ . Blue-solid, green-dashed, red-solid, cyan-solid, purple-dashed, and black-solid curves correspond to  $i_* = 90^\circ, 75^\circ, 60^\circ, 45^\circ, 30^\circ,$  and  $15^\circ$ , respectively.

the largest around the ingress/egress phases, while it is suppressed by the limb darkening depending on the specific values of  $i_{\text{orb}}$  and  $\lambda$ . The modulation term vanishes at the central transit epoch if  $i_{\text{orb}} = 90^\circ$  and/or  $\lambda = 0$  because  $V_{\text{diff}}(0) \propto \cos i_{\text{orb}} \sin \lambda$  as is understood from equation (29).

Figure 9 plots the maximum values of the RM modulation term during the entire transit period as a function of  $i_*$ . If the degree of the differential rotation for the Sun is assumed, the RM effect is supposed to have an additional modulation component of an amplitude of several m/s relative to the rigid rotation case. Given the current precision of the high-resolution radial velocity measurement, it should be detectable for systems with relatively high signal-to-noise ratios.

### 6.3 Uncertainties of the spectroscopic parameters

We have shown that, once the stellar differential rotation effect is taken into account, the precise measurement of the RM velocity anomaly  $\Delta v_{\text{RM}}$  can estimate both the stellar inclination  $i_*$

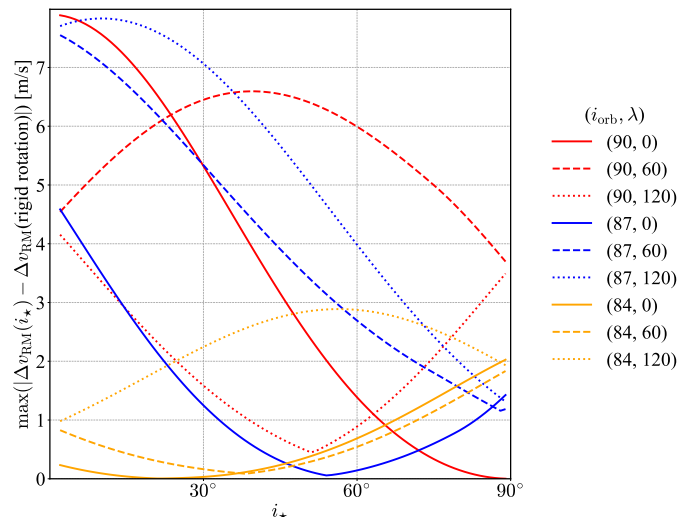


**Fig. 9.** Maximum value of the RM modulation term due to the differential rotation during the entire transit period as a function of  $i_*$  for different values of  $i_{\text{orb}}$  and  $\lambda$  indicated in the legend. We adopt  $\alpha_2 = \alpha_{2\odot}$  and  $\alpha_4 = \alpha_{4\odot}$ . Red, blue, and orange curves assume  $i_{\text{orb}} = 90^\circ$  ( $b = 0$ ),  $87^\circ$  ( $b \approx 0.47$ ), and  $84^\circ$  ( $b \approx 0.93$ ), while solid, dashed and dotted lines correspond to  $\lambda = 0^\circ$ ,  $60^\circ$ , and  $120^\circ$ , respectively.

and the projected spin-orbit angle  $\lambda$ . So far, however, we assumed that the parameters  $\beta$  and  $\zeta$  in equations (34) and (33) are precisely determined from the stellar spectroscopy. In reality, however, the accurate determination of the two parameters is not so easy (e.g., Kamiaka et al. 2018).

Thus it may be possible that the uncertainties of  $\beta$  and  $\zeta$  are degenerate with the stellar differential rotation effect. Since a comprehensive study of the parameter degeneracy is beyond the scope of this paper, we decided to show several examples. Figure 10 plots the dependence on  $\beta$  and  $\zeta$ ; strictly speaking, equations (32), (33), and (34) indicate that  $\Delta v_{\text{RM}}$  depends on the combination of  $\beta^2 + \zeta^2$  under the Gaussian approximation that we adopted throughout the paper. Comparison with Figure 6 implies that while the uncertainties of the spectroscopic parameters distort the RM velocity anomaly curve, the distortion pattern is rather different from the signature due to the differential rotation.

For more quantitative comparison, we plot in Figure 11 the residual of  $\Delta v_{\text{RM}}(\alpha_2, \alpha_4, \beta, \zeta)$  relative to that for the rigid rotation with fiducial spectroscopic parameters, *i.e.*,  $\Delta v_{\text{RM}}(\alpha_2 = \alpha_4 = 0, \beta_{\text{fid}}, \zeta_{\text{fid}})$ . The resulting distortion due to the inaccuracy of the spectroscopic parameter is sensitive to the value of  $\lambda$ , but independent of the value of  $i_*$ , while the signature of the differential rotation model is sensitive to both  $\lambda$  and  $i_*$ . Figure 11 implies that if the RM velocity anomaly is determined with a precision on the order of m/s, one can identify the differential rotation signal even under the presence of a relatively large uncertainty of  $\beta$  and  $\zeta$ .



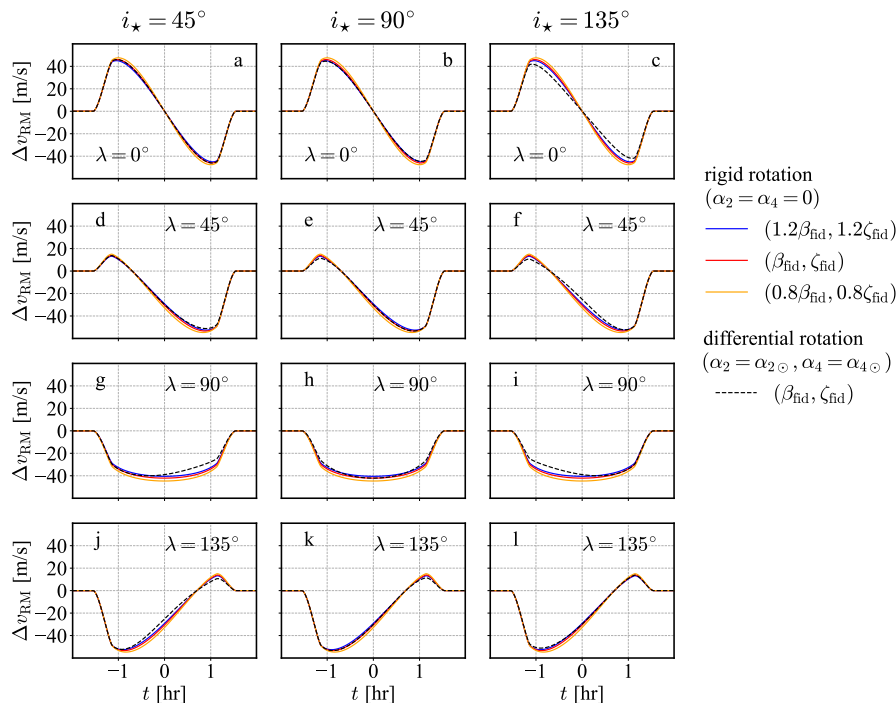


**Fig. 10.** Same as Figure 6 ( $i_{\text{orb}} = 87^\circ$ ), but for different sets of the values of  $\beta$  and  $\zeta$  characterizing the spectroscopic line profiles. Solid lines correspond to the rigid rotation model ( $\alpha_2 = \alpha_4 = 0$ ); blue, red, and orange curves correspond to  $(\beta, \zeta) = (1.2\beta_{\text{fid}}, 1.2\zeta_{\text{fid}})$ ,  $(\beta_{\text{fid}}, \zeta_{\text{fid}})$ , and  $(0.8\beta_{\text{fid}}, 0.8\zeta_{\text{fid}})$ , respectively. For reference, the fiducial differential rotation model ( $\alpha_2 = \alpha_{2\odot}$ ,  $\alpha_4 = \alpha_{4\odot}$ ,  $\beta = \beta_{\text{fid}}$ , and  $\zeta = \zeta_{\text{fid}}$ ) is plotted in dashed curves. The fiducial values of the parameters are summarized in Table 1.

## 7 Summary and conclusions

The Rossiter-McLaughlin (RM) effect has unveiled an unexpected diversity of the spin-orbit architecture of transiting planetary systems. Most of the previous approaches have assumed a rigid rotation of the host star, and thus were not able to estimate the stellar inclination  $i_*$  except for the combination of  $v_* \sin i_*$ . We have improved the previous model of the RM effect by incorporating the differential rotation of the host star. Since our model is fully analytic, it provides a good theoretical understanding of how one can determine  $\lambda$  and  $i_*$  simultaneously from the differential rotation effect.

The latitudinal differential rotation of planetary host stars leaves an additional characteristic signature on the RM effect through equation (28). More specifically, under the Gaussian approximation of stellar lines, the RM effect is analytically described by equation (32), together with equations (33), (34), (45), and (46). We can estimate the values of the spectroscopic parameters,  $\beta_p$  and  $\beta_*$ , and the limb darkening parameters,  $q_1$  and  $q_2$  from photometric and spectroscopic observations of the host star. If the differential rotation of the star is absent, equation (28) vanishes, and equation (27) is specified by  $v_* \sin i_*$  and  $\lambda$ . This provides a widely

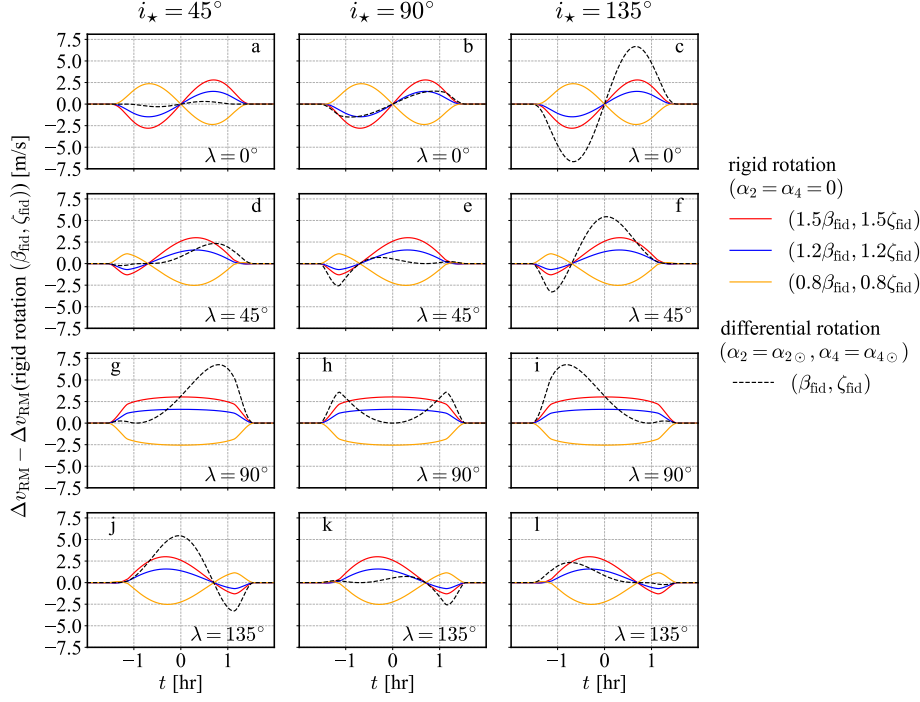


**Fig. 11.** The RM velocity anomaly  $\Delta v_{\text{RM}}(\alpha_2, \alpha_4, \beta, \zeta)$  relative to that for the rigid rotation with fiducial spectroscopic parameters,  $\Delta v_{\text{RM}}(\alpha_2 = \alpha_4 = 0, \beta_{\text{fid}}, \zeta_{\text{fid}})$ . Solid lines correspond to the rigid rotation model ( $\alpha_2 = \alpha_4 = 0$ ); red, blue, and orange curves correspond to  $(\beta, \zeta) = (1.5\beta_{\text{fid}}, 1.5\zeta_{\text{fid}})$ ,  $(1.2\beta_{\text{fid}}, 1.2\zeta_{\text{fid}})$ , and  $(0.8\beta_{\text{fid}}, 0.8\zeta_{\text{fid}})$ , respectively. For reference, the fiducial differential rotation model ( $\alpha_2 = \alpha_{2\odot}$ ,  $\alpha_4 = \alpha_{4\odot}$ ,  $\beta = \beta_{\text{fid}}$ , and  $\zeta = \zeta_{\text{fid}}$ ) is plotted in dashed curves.

used method to estimate the projected spin-orbit angle  $\lambda$  from the RM effect. The differential rotation term, equation (28), makes it possible to estimate  $\alpha_2$ ,  $\alpha_4$  and  $i_*$  separately.

The amplitude of the RM modulation term due to the differential rotation is on the order of several m/s for stars similar to the Sun, and thus should be detectable for systems with reasonably high signal-to-noise ratio of the RM measurement. Therefore, our model is useful in recovering the full spin-orbit angle  $\psi$ , equation (1), based on the RM data analysis alone in principle. In reality, the degeneracy among several parameters might complicate the interpretation of the differential rotation feature in a robust fashion. A preliminary result shown in Figure 11 implies, however, that the uncertainties due of the spectroscopic line profiles are distinguishable from the real differential rotation signature, depending on the values of  $i_*$  and  $\lambda$  of specific systems. We plan to perform a further study of the parameter degeneracy, and to apply the current methodology to a sample of transiting planetary systems, which will be discussed elsewhere.

## Acknowledgements

We thank an anonymous referee and Teruyuki Hirano for many useful and constructive comments. The present work is supported by Grants-in Aid for Scientific Research by the Japan Society for Promotion of Science (JSPS) No.18H012 and No.19H01947, and from JSPS Core-to-core Program “International Network of Planetary Sciences”.

## References

- Albrecht, S. H., Marcussen, M. L., Winn, J. N., Dawson, R. I., & Knudstrup, E. 2021, *ApJL*, 916, L1
- Batygin, K. 2012, *Nature*, 491, 418
- Benomar, O., Masuda, K., Shibahashi, H., & Suto, Y. 2014, *PASJ*, 66, 94
- Boué, G., Montalto, M., Boisse, I., Oshagh, M., & Santos, N. C. 2013, *A&A*, 550, A53
- Brun, A. S., Strugarek, A., Varela, J., Matt, S. P., Augustson, K. C., Emericau, C., DoCao, O. L., Brown, B., & Toomre, J. 2017, *ApJ*, 836, 192
- Casasayas-Barris, N., Palle, E., Stangret, M., Bourrier, V., Tabernerero, H. M., Yan, F., Borsa, F., Allart, R., Zapatero Osorio, M. R., Lovis, C., Sousa, S. G., Chen, G., Oshagh, M., Santos, N. C., Pepe, F., Rebolo, R., Molaro, P., Cristiani, S., Adibekyan, V., Alibert, Y., Allende Prieto, C., Bouchy, F., Demangeon, O. D. S., Di Marcantonio, P., D’Odorico, V., Ehrenreich, D., Figueira, P., Génova Santos, R., González Hernández, J. I., Lavie, B., Lillo-Box, J., Lo Curto, G., Martins, C. J. A. P., Mehner, A., Micela, G., Nunes, N. J., Poretti, E., Sozzetti, A., Suárez Mascareño, A., & Udry, S. 2021, *A&A*, 647, A26
- Fabrycky, D. & Tremaine, S. 2007, *ApJ*, 669, 1298
- Gizon, L. & Solanki, S. K. 2003, *ApJ*, 589, 1009
- Hirano, T., Narita, N., Sato, B., Winn, J. N., Aoki, W., Tamura, M., Taruya, A., & Suto, Y. 2011a, *PASJ*, 63, L57
- Hirano, T., Sanchis-Ojeda, R., Takeda, Y., Narita, N., Winn, J. N., Taruya, A., & Suto, Y. 2012, *ApJ*, 756, 66
- Hirano, T., Suto, Y., Taruya, A., Narita, N., Sato, B., Johnson, J. A., & Winn, J. N. 2010, *ApJ*, 709, 458
- Hirano, T., Suto, Y., Winn, J. N., Taruya, A., Narita, N., Albrecht, S., & Sato, B. 2011b, *ApJ*, 742, 69
- Kamiaka, S., Benomar, O., & Suto, Y. 2018, *MNRAS*, 479, 391
- Kamiaka, S., Benomar, O., Suto, Y., Dai, F., Masuda, K., & Winn, J. N. 2019, *AJ*, 157, 137
- Kipping, D. M. 2013, *MNRAS*, 435, 2152

Kozai, Y. 1962, *AJ*, 67, 591

Lidov, M. L. 1962, *Planet. Space Sci.*, 9, 719

Lin, D. N. C., Bodenheimer, P., & Richardson, D. C. 1996, *Nature*, 380, 606

Louden, E. M., Winn, J. N., Petigura, E. A., Isaacson, H., Howard, A. W., Masuda, K., Albrecht, S., & Kosiarek, M. R. 2021, *AJ*, 161, 68

McLaughlin, D. B. 1924, *ApJ*, 60, 22

Nagasawa, M. & Ida, S. 2011, *ApJ*, 742, 72

Nagasawa, M., Ida, S., & Bessho, T. 2008, *ApJ*, 678, 498

Ohta, Y., Taruya, A., & Suto, Y. 2005, *ApJ*, 622, 1118

Queloz, D., Eggenberger, A., Mayor, M., Perrier, C., Beuzit, J. L., Naef, D., Sivan, J. P., & Udry, S. 2000, *A&A*, 359, L13

Rasio, F. A. & Ford, E. B. 1996, *Science*, 274, 954

Rossiter, R. A. 1924, *ApJ*, 60, 15

Snodgrass, H. B. & Ulrich, R. K. 1990, *ApJ*, 351, 309

Takaishi, D., Tsukamoto, Y., & Suto, Y. 2020, *MNRAS*, 492, 5641

Valenti, J. A. & Fischer, D. A. 2005, *ApJS*, 159, 141

Winn, J. N. & Fabrycky, D. C. 2015, *ARA&A*, 53, 409

Winn, J. N., Noyes, R. W., Holman, M. J., Charbonneau, D., Ohta, Y., Taruya, A., Suto, Y., Narita, N., Turner, E. L., Johnson, J. A., Marcy, G. W., Butler, R. P., & Vogt, S. S. 2005, *ApJ*, 631, 1215

Xue, Y., Masuda, K., & Suto, Y. 2017, *ApJ*, 835, 204

Xue, Y., Suto, Y., Taruya, A., Hirano, T., Fujii, Y., & Masuda, K. 2014, *ApJ*, 784, 66